Int. J. Solids Structures Vol. 24, No. 11, pp. 1113–1130, 1988
Printed in Great Britain.

0020-7683/88 $3.00+.00

STRESS–STRAIN HISTORIES IN COATINGS ON SINGLE CRYSTAL SPECIMENS OF A TURBINE BLADE ALLOY

ESTEBAN P. BUSSO and FRANK A. MCCLINTOCK
Department of Mechanical Engineering, Massachusetts Institute of Technology, Cambridge, MA 02139, U.S.A.

(*Received* 18 *November* 1987; *in revised form* 5 *May* 1988)

Abstract—The stress–strain response of an electron beam, physical vapor deposited (EB-PVD) NiCoCrAlY overlay coating applied to a single crystal nickel base superalloy (CMSX-3) is studied by subjecting stepped-disk fatigue specimens to thermal cycles with different rates of heating (from 520 to 1090°C in 4.5, 6, and 20 s) and cooling (to 520°C in 7 and 15 s). Rate-dependent material anisotropy is modelled using a creep (or flow) potential for a cubic crystal and the associated flow rule. An anisotropic creep finite element analysis of the substrate reveals that continued cycling does not affect the strain ranges, which play a role in coating degradation. However, continued cycling does produce an increase of the peak tensile stresses (from 13 MPa for the first cycle to about 250 MPa at the 6000th cycle for 4.5 s heating history). Most of this transition occurs before the 500th cycle. As a consequence of these tensile stresses, crack propagation rates into the substrate are expected to be more severe than the predictions from a thermo-elastic analysis. However, the conventional thermo-elastic analysis is very accurate at estimating the strain ranges. For the coating, an isotropic creep finite element analysis shows that the mechanical strain range ($\Delta\varepsilon^c + \Delta\varepsilon^c$) and tensile peak stresses responsible for crack initiation and crack growth, with 0.52% strain range in the substrate, are 0.83% and 460 MPa for the 4.5 s heating cycle, due in large part to the thermal expansion mismatch between the coating and substrate.

1. INTRODUCTION

The drive toward better performance and fuel economy for aircraft gas turbine engines has resulted in ever-higher turbine inlet temperatures. The resulting heating and cooling rates are higher along the airfoil edges than in the bulk of the blade, generating cyclic thermal strain gradients. During take-off the leading and trailing edges of a first stage blade can rise from 520 to 1090°C in under 8 s (Thulin *et al.*, 1982; Kaufman and Halford, 1984). During turbine shut-down immediately after landing and thrust reverse, the edge temperatures can decrease from 1090 to 520°C in 5–17 s.

The choice of the substrate material is usually based on its creep and fatigue strengths for given operating conditions. Material chemistry may enhance these mechanical properties but does little to improve resistance against oxidation, hot corrosion, and surface erosion experienced by materials at high temperatures. This deficiency is overcome by applying a 50–100 μm thick protective coating. However, the ever-increasing operating conditions make coating degradation a life-limiting phenomenon.

Knowledge of the stress–strain histories of both the substrate (e.g. blades by Kaufman and Halford (1984)) and the coating is necessary to predict how these histories cause coating cracking or spalling, reducing its ability to protect the substrate. Unfortunately, direct measurements of stresses and strains during service are not possible. Therefore, simulation of service conditions with feasible experiments is necessary. Furthermore, due to interaction between material properties and the inhomogeneous temperatures, these experiments are usually coupled with highly complex analysis.

Considerable work has been done in the past on thermal fatigue of uncoated (Howes, 1976) and coated specimens (Leverant *et al.*, 1976; Nesbitt *et al.*, 1984; Rickerby and Wood, 1986). However, many limitations arise from the gas burner and fluidized bed techniques used to simulate service conditions. During this investigation, induction heating of the periphery of coated stepped-disk specimens was used to reproduce heating rates and ranges of cyclic thermal strains typical of those developed in trailing edges of blades and vanes during normal operating conditions. This technique, developed by Holmes *et al.*

Table 1. Nominal chemical compositions of substrate and coating

		Ni	Co	Cr	Mo	W	Ti	Al	Ta	Y
CMSX-3 substrate (MAR-M-247 derivative)	wt. %	66.4	4.6	7.9	0.5	8.0	1.0	5.6	6.0	—
	at. %	67.9	4.7	9.1	0.3	2.6	1.1	12.4	1.9	—
NiCoCrAlY coating	wt. %	50	20	18	—	—	—	12	—	0.2
	at. %	42.4	17.6	17.8	—	—	—	22	—	0.05

(1987), and adapted to 14 mm diameter specimens by Busso (1987), offers substantial improvements over the more traditional gas burner and fluidized bed techniques (Howes, 1976). The main advantages of induction heating are reduced costs and the increased flexibility in selecting the desired temperature cycle and the environment to which the specimens will be subjected. As in gas burner rigs and fluidized bed tests, the temperatures can be measured with appropriately placed thermocouples. This eliminates the need for expensive heat transfer analysis to determine the temperature distributions in the specimen during the thermal cycle.

Here we address the problem of finding the coating strain histories due to imposed loading from the substrate under various heating and cooling rates in the convenient disk-shaped specimens used with induction heating. Accompanying thermal fatigue experiments have been reported elsewhere (Busso, 1987; Busso and McClintock, 1988).

As an example, CMSX-3 was chosen as a typical precipitation hardened Ni-based superalloy. An electron beam, physical vapor deposited (EB-PVD) NiCoCrAlY overlay coating was selected as the protective coating (see Table 1 for chemical compositions).

2. EXPERIMENTAL PROCEDURE

2.1. *Specimen Geometry*

Stepped-disk specimens of 14 mm diameter (Fig. 1) were machined from a single crystal rod of CMSX-3 with their faces normal to the ⟨001⟩ crystal growth direction and

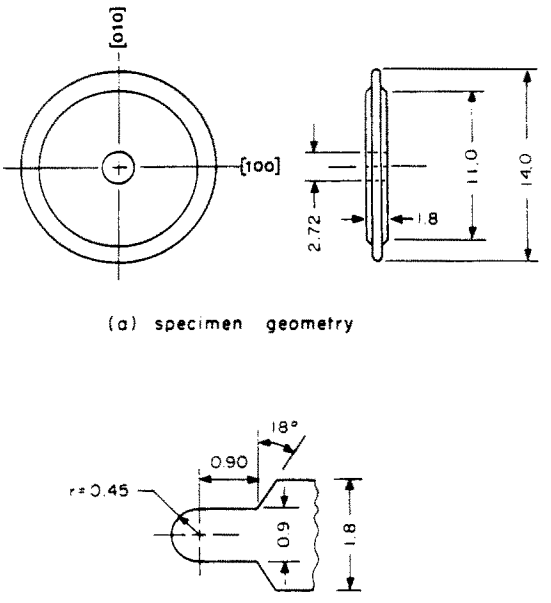

Fig. 1. Detailed drawing and orientation of stepped-disk specimen (all dimensions in mm). After Holmes *et al.* (1987).

with external radii typical of those of blade trailing edges. Specimens were subsequently given a 95 μm thick coating and a combined aging and diffusion treatment.

Due to the anisotropic elastic and creep material properties interacting with the radially inhomogeneous temperatures, the strain range along the specimen periphery is a function of its local crystallographic orientation, changing from a maximum at the $\langle 100 \rangle$ to a minimum at the $\langle 110 \rangle$ periphery orientation. This allows the use of a single specimen to simultaneously obtain coating durability and crack initiation data from various strain levels, all subject to the same temperature histories.

2.2. *Control of Coating Strain History*

Since the thin coating gives negligible constraints to the substrate, the total in-plane strain history of the coating is determined by the total in-plane strain history of the substrate.

Programming of the power input to the concentrator coil allows control of the heating and cooling rates. These rates in turn determine the transient strains in the periphery from the temperature distributions throughout the specimen. Enough steady state compression in the periphery to simulate cruise conditions is achieved by passing compressed air through the center of the specimen and its supporting rods.

For higher tensile strains during cooling, high pressure air was blown on the specimen periphery from an upper and a lower cooling manifold (Holmes *et al.*, 1987).

2.3. *Selection of Thermal Cycles*

To determine the effect of different strain histories on coating degradation, three different heating rates were used on the periphery, all with minimum temperatures of 520°C, a holding time of 60 s at 1090°C, and cooling back to 520°C in 15 s. The rapid 4.5 s heating of Fig. 2(a), the intermediate 6 s of Fig. 2(b), and the slow 20 s heating cycle of Fig. 2(c) were chosen to show how the strain histories obtained from these different cycles affect coating life. The intermediate heating (6 s) rate was combined with a fast cooling (7 s) rate to evaluate the effect of higher tensile peak stresses generated during cycle cooling (Fig. 2(d)). The temperature profiles in the specimen were established by using four chromel–alumel thermocouples (0.13 mm wire diameter) at various radii (Fig. 3).

3. FINITE ELEMENT ANALYSIS

In the disk-shaped specimen discussed here, the stress–strain history of its periphery is found from the measured temperature history throughout the specimen. The non-linear finite-element program ABAQUS (1985) was used for this purpose.

It is common practice in industry to use elastic strain ranges as a way to describe coating conditions. In general, a high temperature component is subjected to both static (creep) and cyclic (fatigue) loadings. A flow and evolutionary model for a general history in the Bauschinger regime ($\varepsilon < 1\%$) would be needed to account for all types of inelastic strains which develop during service. However, due to the lack of such data, anisotropic power law creep was assumed as an initial approximation to determine the effects of inelasticity on the stress–strain response, compared with a thermo-elastic analysis.

3.1. *Model of Substrate*

Due to symmetry, a 45° octant of the anisotropic stepped-disk specimen was sufficient for finite element modelling (Fig. 3). One hundred and twelve eight-node plane stress elements with full Gaussian integration were used. Symmetry boundary conditions were applied along the $\langle 100 \rangle$ and $\langle 110 \rangle$ radial directions.

The mean coefficients of thermal expansion for the single crystal CMSX-3 are given in Fig. 4 (Allison–GM, 1986).

Elastic compliance data, determined ultrasonically (Allison–GM, 1986), were given in terms of

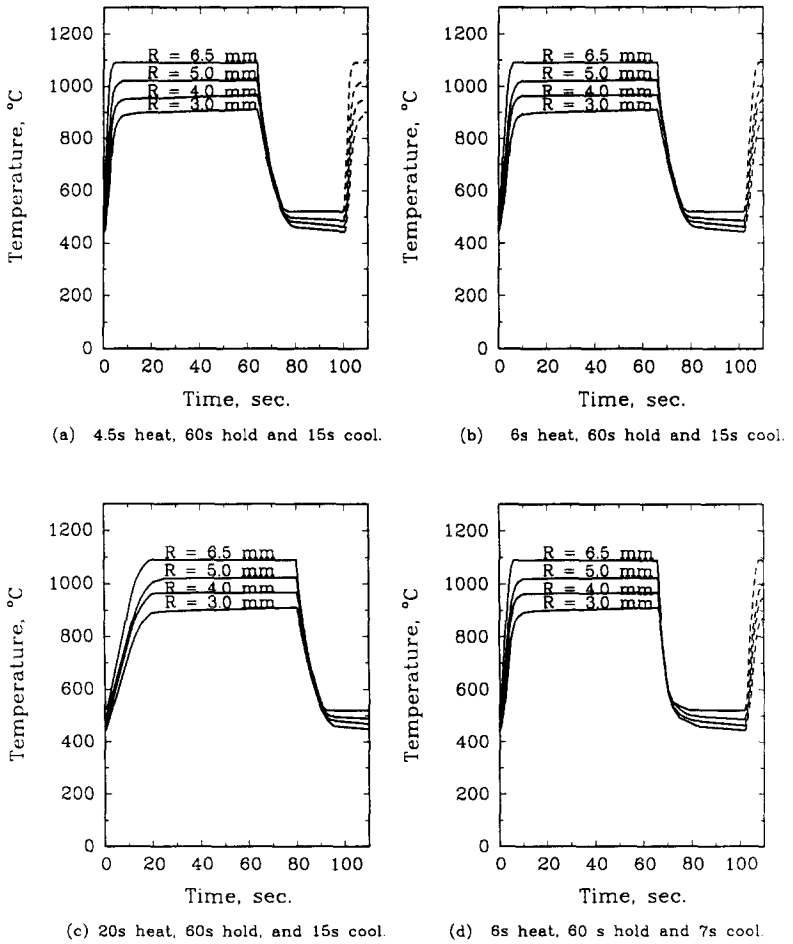

Fig. 2. Radial temperature distributions in specimen when its periphery temperature is cycled from 520 to 1090°C.

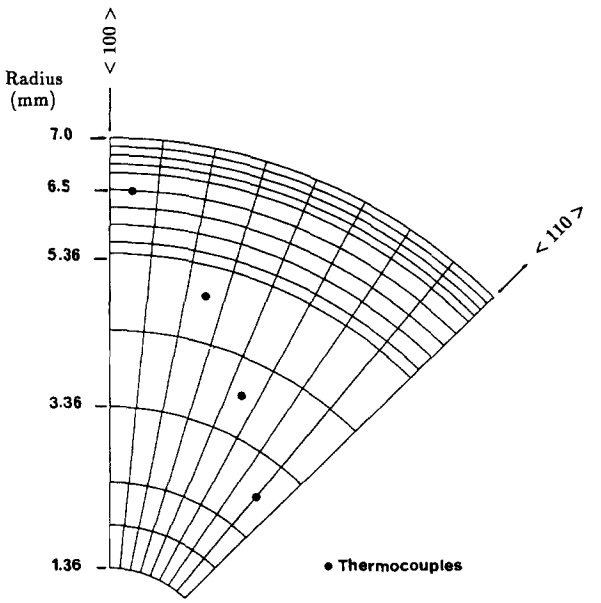

Fig. 3. Finite element mesh of stepped-disk specimen.

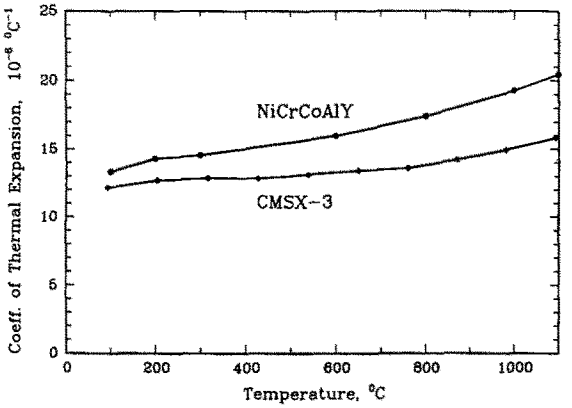

Fig. 4. Coefficients of thermal expansion for the substrate (CMSX-3) and coating (NiCoCrAlY). (Reference temperature = 25°C.)

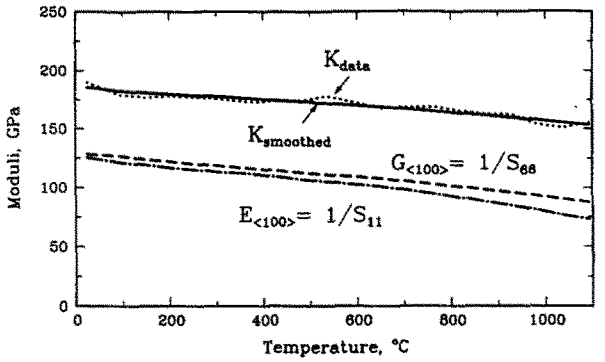

Fig. 5. Original and smoothed bulk modulus K, Young's modulus, and shear modulus for ⟨100⟩ crystal orientation.

$$S_{11} = \frac{1}{E_{\langle 100\rangle}} \quad S_{12}, \quad \text{and} \quad S_{66} = \frac{1}{G_{\langle 100\rangle}}. \tag{1}$$

Because the bulk modulus K, determined from

$$K = \frac{1}{3(S_{11}+2S_{12})} \tag{2}$$

showed some irregularities (Fig. 5), the data were smoothed with a second-order polynomial. These smoothed values, together with $E_{\langle 100\rangle}$ and $G_{\langle 100\rangle}$, were then used to obtain the elastic compliances. For cubic symmetry, the stiffness constants denoted E_{ijkl} in ABAQUS (1985) are related to the usual two-index stiffness constants C_{ij} and the compliance components S_{ij} by

$$E_{1111} = E_{2222} = E_{3333} = C_{11} = \frac{S_{11}+S_{12}}{(S_{11}-S_{12})(S_{11}+2S_{12})}$$

$$E_{1122} = E_{1133} = E_{2233} = C_{12} = \frac{-S_{12}}{(S_{11}-S_{12})(S_{11}+2S_{12})}$$

$$E_{1212} = E_{1313} = C_{66} = C_{44} = \frac{1}{S_{44}}. \tag{3}$$

The final elastic stiffnesses C_{ij} are given in Fig. 6.

The steady state creep data from ⟨100⟩ specimens of Table 2 (Allison–GM, 1986), provided at 1010 and 1066°C, were expressed in terms of the relation

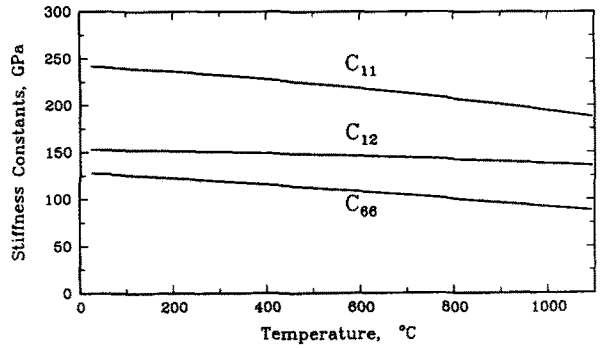

Fig. 6. Stiffness constants C_{ij} vs temperature for CMSX-3.

Table 2. Creep coefficients of eqn (4) for CMSX-3

T (°C)	$\dot{\varepsilon}_0$ (s^{-1})	m
1010	1.209×10^{-7}	8.27
1066	5.734×10^{-7}	8.06

$$\dot{\varepsilon}_{ss} = \dot{\varepsilon}_R \, e^{-Q/RT} \left(\frac{\sigma}{\sigma_0}\right)^{m(T)} = \dot{\varepsilon}_0(T) \left(\frac{\sigma}{\sigma_0}\right)^{m(T)} \tag{4}$$

where the nominal strength $\sigma_0 (= 200$ MPa) is the stress at which the creep activation energy of 397 kJ mol^{-1} was found from a plot of ln $\dot{\varepsilon}_0$ vs $1/T$. In ABAQUS (1985), the resulting $\dot{\varepsilon}_0(T)$ was linearly interpolated within 10°C intervals, with a maximum relative error of 3%.

3.2. *Creep Anisotropy*

3.2.1. *Hill's stress function*

For creep anisotropy, ABAQUS (1985) employs a generalization of the Mises yield criterion proposed by Hill (1950), which for axes with cubic symmetry is given in terms of a parameter R ($= 1$ for isotropy)

$$\bar{\sigma}^2 = \tfrac{1}{2}[(\sigma_{22}-\sigma_{33})^2+(\sigma_{11}-\sigma_{22})^2+(\sigma_{33}-\sigma_{11})^2]+3R[\sigma_{23}^2+\sigma_{31}^2+\sigma_{12}^2]. \tag{5}$$

Equation (5) can also be expressed in terms of stress deviators, defined as the differences of normal components from the mean normal stress $s_{ij} \equiv \sigma_{ij}-\delta_{ij}\sigma$, where $\sigma \equiv \sigma_{ii}/3$

$$\begin{aligned}\bar{\sigma}^2 &= \tfrac{3}{2}s_{ij}s_{ij}|_{(i=j)}+\tfrac{3}{2}Rs_{ij}s_{ij}|_{(i\neq j)} \\ &= \tfrac{3}{2}(s_{11}^2+s_{22}^2+s_{33}^2)+\tfrac{3}{2}R(s_{12}^2+s_{21}^2+s_{23}^2+s_{32}^2+s_{31}^2+s_{13}^2).\end{aligned} \tag{6}$$

The shear stress components σ_{12} (relative to cubic, ⟨100⟩, axes) will be different from zero primarily near the ⟨110⟩ axes, so that R affects the creep rates in that region. To find R, a functional relation between it and the available ⟨100⟩ and ⟨110⟩ creep data must be developed.

3.2.2. *The associated flow rule*

The fact that the strain increment vector associated with a given point on the yield locus must always be normal to the locus† (derived by Bishop and Hill (1951) from the resolved shear stress law for all slip systems within a crystal, a polycrystal, or a structure) implies that there is a proportionality between components of plastic strain increment and the corresponding components of the outward normal to the yield locus in the stress space. This relation is called *the associated flow rule*. For incompressible materials (with strains equal to strain deviators) it gives the strain increments in terms of the stress deviators, partial derivatives, and a proportionality constant $d\lambda$

† Except at any sharp corner on the yield surface.

$$d\varepsilon_{ij}^{p} = \frac{\partial \bar{\sigma}}{\partial s_{ij}} d\lambda. \tag{7}$$

Differentiating the stress function $\bar{\sigma}$ in the form of eqn (6) gives the anisotropic stress–strain relations

$$d\varepsilon_{11}^{p} = \frac{\partial \bar{\sigma}}{\partial s_{11}} d\lambda = \frac{1}{2\bar{\sigma}} \frac{\partial \bar{\sigma}^2}{\partial s_{11}} d\lambda = \tfrac{3}{2} s_{11} \frac{d\lambda}{\bar{\sigma}}, \quad d\varepsilon_{22}^{p} = \cdots$$

$$d\gamma_{12}^{p} = 2d\varepsilon_{12}^{p} = 2\frac{\partial \bar{\sigma}}{\partial s_{12}} d\lambda = \frac{1}{\bar{\sigma}} \frac{\partial \bar{\sigma}^2}{\partial s_{12}} d\lambda = 3Rs_{12} \frac{d\lambda}{\bar{\sigma}}, \ldots \tag{8}$$

Note that the one-to-one relationship between $d\varepsilon_{ij}^{p}$ and the corresponding component s_{ij} is only true for materials which exhibit isotropic or cubic anisotropic behavior.

Finding the proportionality constant $d\lambda$. The plastic work done as a body undergoes deformation can be thought of as the dot product of the deviatoric stress and plastic strain increment

$$\begin{aligned} dW^{p} &= s_{ij}\, d\varepsilon_{ij} \\ &= s_{11}\, d\varepsilon_{11}^{p} + s_{22}\, d\varepsilon_{22}^{p} + s_{33}\, d\varepsilon_{33}^{p} + 2s_{23}\, d\varepsilon_{23}^{p} + 2s_{31}\, d\varepsilon_{31}^{p} + 2s_{12}\, d\varepsilon_{12}^{p}. \end{aligned} \tag{9}$$

Now substituting eqn (8) into eqn (9)

$$dW^{p} = \frac{d\lambda}{\bar{\sigma}} [\tfrac{3}{2}(s_{11}^2 + s_{22}^2 + s_{33}^2) + 3R(s_{23}^2 + s_{31}^2 + s_{12}^2)] = \frac{d\lambda}{\bar{\sigma}} \bar{\sigma}^2. \tag{10}$$

An increment in equivalent plastic strain can thus be defined as the work per unit equivalent stress

$$d\lambda = \frac{dW^{p}}{\bar{\sigma}} \equiv d\bar{\varepsilon}^{p}. \tag{11}$$

For creep, rates rather than strain increments must be described. Equation (8), with $d\lambda$ replaced by $d\bar{\varepsilon}^{p}$ from eqn (11) becomes

$$\dot{\varepsilon}_{11}^{p} = \tfrac{3}{2} s_{11} \frac{\dot{\bar{\varepsilon}}^{p}}{\bar{\sigma}}, \ldots, \quad \dot{\gamma}_{12}^{p} = 3Rs_{12} \frac{\dot{\bar{\varepsilon}}^{p}}{\bar{\sigma}}, \ldots \tag{12}$$

We assume that $\dot{\bar{\varepsilon}}^{p}$ follows power law creep

$$\dot{\bar{\varepsilon}}^{p} = \dot{\varepsilon}_0 \left(\frac{\bar{\sigma}}{\sigma_0} \right)^{m}. \tag{13}$$

3.2.3. *Finding R from uniaxial* $\langle 100 \rangle$ *and* $\langle 110 \rangle$ *creep data*

Loading along a $\langle 100 \rangle$ *orientation.* The applied stress $\sigma_{\langle 100 \rangle}$ gives a longitudinal creep rate $\dot{\varepsilon}_{11}^{p}$ (in cubic axes). From the power law relation of eqn (13), with $\bar{\sigma} = \sigma_{\langle 100 \rangle}$ and $\dot{\varepsilon}_{11}^{p} = \dot{W}^{p}/\sigma_{\langle 100 \rangle} = \dot{\bar{\varepsilon}}^{p}$

$$\dot{\varepsilon}_{11}^{p} = \dot{\varepsilon}_0 \left(\frac{\sigma_{\langle 100 \rangle}}{\sigma_0} \right)^{m}. \tag{14}$$

Loading along a $\langle 110 \rangle$ *orientation.* Here there is no cubic symmetry, so the yield locus is no longer represented by the cubic form of Hill's yield function (5). To avoid having to

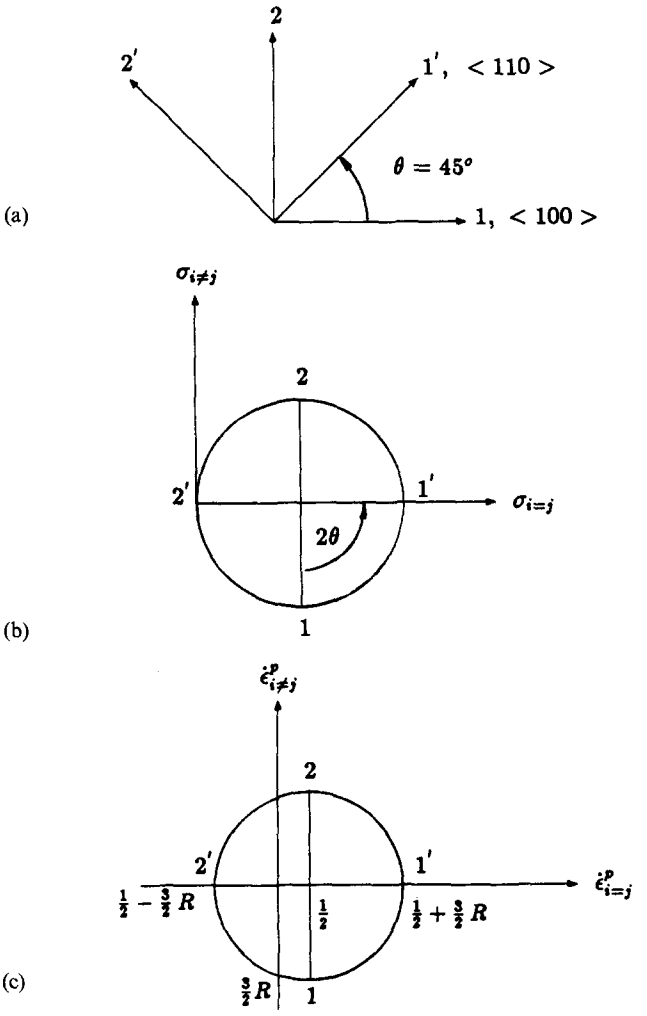

Fig. 7. (a) Physical plane. (b) Stress plane. (c) Strain (rate) plane, units of $\dot{\varepsilon}^p/(1+3R)^{-1/2}$.

find a new yield function for this orientation, we rotate the reference frame back to cubic axes. The stress field in a $\langle 110\rangle$ specimen (system 1′–2′ of Fig. 7(a)) is

$$\sigma_{1'1'} = \sigma_{\langle 110\rangle} \neq 0, \quad \sigma_{2'2'} = \sigma_{3'3'} = 0.$$

Now finding the stress components for the cubic axes (system 1–2 of Fig. 7(a)) through Mohr's circle of Fig. 7(b)

$$\sigma_{11} = \sigma_{22} = \sigma_{12} = \frac{\sigma_{\langle 110\rangle}}{2}. \tag{15}$$

The mean normal stress is

$$\sigma = \frac{\sigma_{11}+\sigma_{22}}{3} = \frac{\sigma_{\langle 110\rangle}}{3}$$

and the deviatoric components of eqn (15) are

$$\epsilon_{ij}^{applied}(t) = \epsilon_{ij}^{e}(t) + \epsilon_{ij}^{c}(t) + \epsilon_{ij}^{th}(t)$$

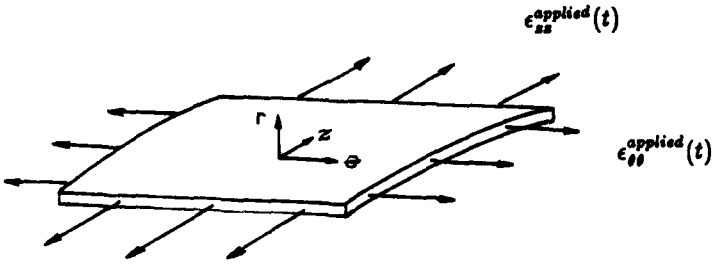

Fig. 8. Model of coating.

$$s_{11} = s_{22} = \frac{\sigma_{\langle 110\rangle}}{6}, \quad s_{33} = -\frac{\sigma_{\langle 110\rangle}}{3}, \quad s_{12} = s_{21} = \frac{\sigma_{\langle 110\rangle}}{2}. \tag{16}$$

Substituting eqns (16) into eqn (6) gives the equivalent stress in cubic axes in terms of the applied stress $\sigma_{\langle 110\rangle}$ and R

$$\bar{\sigma}^2 = \frac{\sigma_{\langle 110\rangle}^2}{4}(1+3R). \tag{17}$$

To find the strain rates in cubic axes, substitute eqns (16) and (17) into eqns (12)

$$\dot{\varepsilon}_{11}^{p} = \dot{\varepsilon}_{22}^{p} = \frac{3}{2}\frac{\sigma_{\langle 110\rangle}}{6}\frac{2}{\sigma_{\langle 110\rangle}(1+3R)^{1/2}}\dot{\bar{\varepsilon}}^{p} = \frac{1}{2}\frac{1}{(1+3R)^{1/2}}\dot{\bar{\varepsilon}}^{p}$$

$$\dot{\varepsilon}_{33}^{p} = -\dot{\varepsilon}_{11}^{p} - \dot{\varepsilon}_{22}^{p} = -\frac{1}{(1+3R)^{1/2}}\dot{\bar{\varepsilon}}^{p}$$

$$\dot{\gamma}_{12}^{p} = 3R\frac{\sigma_{\langle 110\rangle}}{2}\frac{2}{\sigma_{\langle 110\rangle}(1+3R)^{1/2}}\dot{\bar{\varepsilon}}^{p} = 3R\frac{1}{(1+3R)^{1/2}}\dot{\bar{\varepsilon}}^{p}. \tag{18}$$

Using Mohr's circle once again (Fig. 7(c)), gives the $\langle 110\rangle$ creep rates from the $\langle 100\rangle$ rates of eqns (18) in terms of the $\langle 100\rangle$ equivalent strain rate $\dot{\bar{\varepsilon}}^{p}(\bar{\sigma})$

$$\dot{\varepsilon}_{1'1'}^{p} = (\tfrac{1}{2}+\tfrac{3}{2}R)\frac{1}{(1+3R)^{1/2}}\dot{\bar{\varepsilon}}^{p}(\bar{\sigma}). \tag{19}$$

Expressing $\dot{\bar{\varepsilon}}^{p}(\bar{\sigma})$ in terms of $\bar{\sigma}$ from power law creep (13) and $\bar{\sigma}$ in terms of $\sigma_{\langle 110\rangle}$ from eqn (17)

$$\dot{\varepsilon}_{1'1'}^{p} = \left(\frac{\sqrt{(1+3R)}}{2}\right)^{m+1}\dot{\varepsilon}_0\left(\frac{\sigma_{\langle 110\rangle}}{\sigma_0}\right)^{m}. \tag{20}$$

Substituting $\dot{\varepsilon}_0$ and σ_0 from eqn (14) into eqn (20) and replacing $\dot{\varepsilon}_{11}^{p}$ of eqn (14) by the identical $\dot{\varepsilon}_{\langle 100\rangle}^{p}$ gives R from $\langle 100\rangle$ and $\langle 110\rangle$ creep data

$$\dot{\varepsilon}_{1'1'}^{p} = \dot{\varepsilon}_{\langle 110\rangle}^{p} = \left(\frac{\sqrt{(1+3R)}}{2}\right)^{m+1}\left(\frac{\sigma_{\langle 110\rangle}}{\sigma_{\langle 100\rangle}}\right)^{m}\dot{\varepsilon}_{\langle 100\rangle}^{p}. \tag{21}$$

$\langle 110\rangle$ and $\langle 100\rangle$ creep data (Allison–GM, 1986), taken at 1090°C, gave $R = 1.13$.

3.3. *Model of the Coating*

Since in a thin coating the stress and strain rate are homogeneous, the coating was modelled with a single four-node plane stress element. The plane of the model was the (traction-free surface) r plane of the substrate coordinates (Fig. 8). Since the in-plane

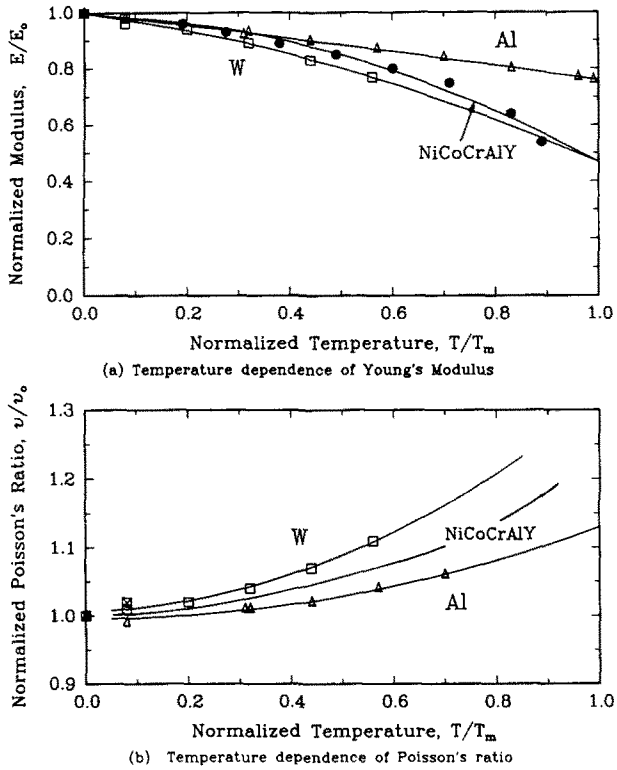

Fig. 9. Interpolation of Poisson's ratio for NiCoCrAlY from Al and W data. (Temperature normalized with the melting point, E and ν normalized with their values at 0 K.)

components of displacements are the same in both the coating and substrate, they determine the in-plane components of total strain (the tangential $\varepsilon_{\theta\theta}^{\text{applied}}(t)$ and the through-specimen-thickness $\varepsilon_{zz}^{\text{applied}}(t)$ strain components of Fig. 8) in the coating, which constitute its imposed loads. The $\varepsilon_{zz}^{\text{applied}}(t)$ component can be conveniently found by modelling the external row of elements of Fig. 3 with generalized plane strain elements with $\sigma_{zz} = 0$. The temperature history for the coating was that of the outer radius of the specimen for the most severe heating time, 4.5 s (Fig. 2(a) at $R = 6.5$ mm).

The NiCoCrAlY coating was assumed isotropic. Its elastic dynamic modulus was obtained from Hillery *et al.* (1986) and fitted with a second-order polynomial as shown in Fig. 9(a). Due to the lack of accurate data, Poisson's ratio at high temperatures for the NiCoCrAlY had to be approximated from the ratios for materials which exhibit similar homologous temperature dependence in Young's modulus. Comparison of available modulus data for several materials (Simmons and Wang, 1971) showed the NiCoCrAlY to have similar temperature dependence to Al and W (Fig. 9(a)). The elastic modulus and Poisson's ratio were normalized by dividing their values at zero absolute temperature, and the temperature by the melting point temperature, T_m. Figure 9(b) shows Al and W Poisson's ratio as well as the interpolated values for NiCoCrAlY. The mean coefficient of thermal expansion for the isotropic NiCoCrAlY coating is given in Fig. 4 (Allison–GM, 1986).

The creep behavior was modelled from data at 661, 850 and 1050 C obtained by Hebsur and Miner (1986) on a plasma sprayed NiCoCrAlY coating. In order to interpolate creep data at intermediate temperatures logarithmically and to avoid occasional narrow-band temperature interpolation inaccuracies, a user's material subroutine containing the power law creep model and a forward gradient time-integration procedure was implemented.

4. RESULTS AND DISCUSSION

4.1. *Substrate*

4.1.1. *Anisotropic thermo-elastic analysis*

A feeling for the stress–strain histories can be obtained by following the cycle of Fig.

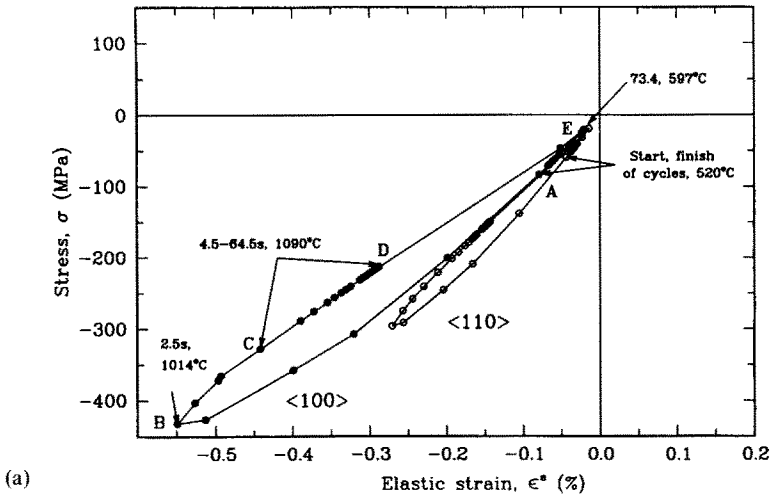

(a)

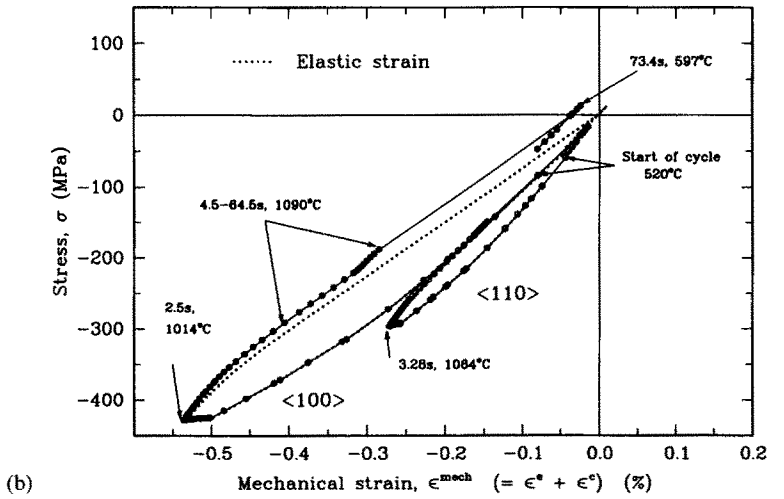

(b)

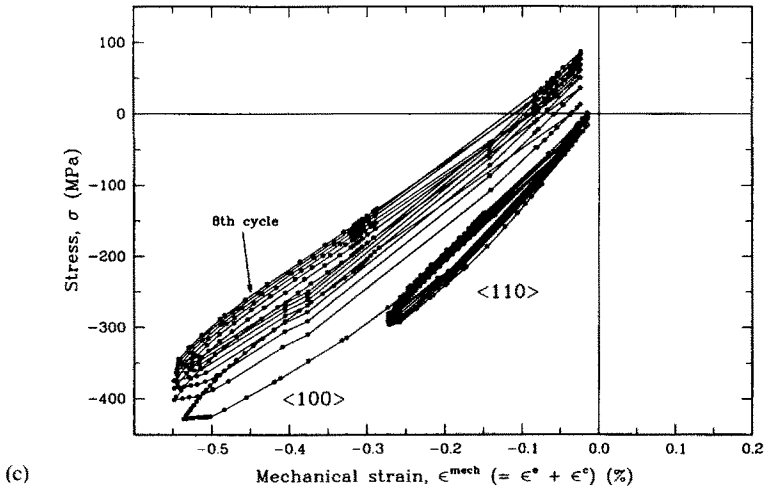

(c)

Fig. 10. Stress–strain hysteresis loops of the specimen rim in the ⟨100⟩ and ⟨110⟩ orientations for 4.5 s heating cycle: (a) thermo-elastic analysis; (b) anisotropic creep analysis, first cycle; (c) anisotropic creep analysis, later cycles.

Table 3. Comparison of substrate thermo-elastic and creep analyses

Cycle (s)	Rim orientation	Anisotropic creep (eighth cycle) Strain history (%) ε^{cr}_{min}	Range, $\Delta\varepsilon^{cr}$	Cooling stress (MPa) σ^{cr}_{max}	Thermo-elastic Cooling stress (MPa) σ^{el}_{max}
20–15	⟨110⟩	−0.169	0.152	−10	−19
20–7	⟨110⟩	−0.165	0.180	26	22
6–15	⟨110⟩	−0.213	0.197	−5	−16
4.5–15	⟨110⟩	−0.273	0.258	−1	−1
20–15	⟨100⟩	−0.333	0.304	45	−21
20–7	⟨100⟩	−0.334	0.356	98	27
6–15	⟨100⟩	−0.425	0.399	60	−20
4.5–15	⟨100⟩	−0.543	0.519	87	−20

10(a). For the ⟨100⟩ rim orientation, the initial heating drives the rim into compression (A to B). From B to C, although the temperature is still increasing, the stresses become less compressive due to a decrease in the radial temperature gradient. (The sharp corner at B is due to the discrete time–temperature input in the finite element model.) From C to D, the rim temperature is kept constant at 1090°C but the core temperature is still rising and the rim stress is becoming less compressive, both approaching the steady-state D after only 10–20 s.

Cooling decreases the compressive stresses, and with fast cooling (7 s), they even become tensile (see last column of Table 3). After this peak at E, the material starts unloading elastically until the beginning of the next cycle at A. The peak cooling stress σ_{max} will be discussed further in connection with the creep analysis. A similar behavior is observed at the ⟨110⟩ rim orientation (Table 3).

4.1.2. *Anisotropic creep analysis*

Since fatigue and fracture are unaffected by the thermal strains *per se*, the results of the creep analysis will be discussed in terms of the mechanical strains, $\varepsilon^{mech} \equiv \varepsilon^{e} + \varepsilon^{c} = \varepsilon^{T} - \varepsilon^{th}$.

(1) The extreme strains and the strain ranges at both ⟨100⟩ and ⟨110⟩ locations are hardly affected by creep, as shown by comparing the thermo-elastic cycle with the first creep cycle in Fig. 10(b) and with successive creep cycles in Figs 10(c), 11 and 12.

(2) The shape of the hysteresis loops remains relatively unchanged by creep, as shown in Figs 10–12 (the break in the slope during heating for cycles after the first one, at $\varepsilon^{mech} = 0.3\%$, is due to having increased the tolerance for the solution of the equilibrium equations for economy in running eight thermal cycles). Furthermore, the strain range remains almost constant, showing a change of less than 2% between the first and eighth cycle for any given thermal history.

(3) For the ⟨100⟩ rim location, continued cycling produces ratcheting of the hysteresis loop (Figs 10–12). The peak compressive and tensile strains and the stress range remain nearly constant, but the peak cooling *stress* increases, shifting the loop upward. To see the source of the shift, compare the elastic and creep strains during the first cycle for the 4.5 s history (Fig. 10(b)). Significant compressive creep begins at about 1010°C, increasing the mean stress of the cycle. The compressive stress then decreases rapidly with only slightly increasing temperatures, reducing the creep rate. For the first cycle, approximately half of the creep strains accumulate in the first few seconds after 1000°C is reached (e.g. Fig. 10(b)). The remaining half of the creep accumulates during simulated cruise conditions at constant temperature. This stress relaxation diminishes as the cycles shift to higher peak cooling stresses.

Since the tensile stresses introduced during cooling take place at temperatures below those where creep and stress relaxation occur and are insufficient to cause yield (according to data from Mackay *et al.* (1980)), such cooling involves only elastic strains. These high tensile stresses would accelerate the crack propagation into the substrate. This may be critical if a cracked substrate could perform its functions for a limited length of time.

(4) To estimate the long-time ratcheting of the ⟨100⟩ cooling stress, a mechanics-

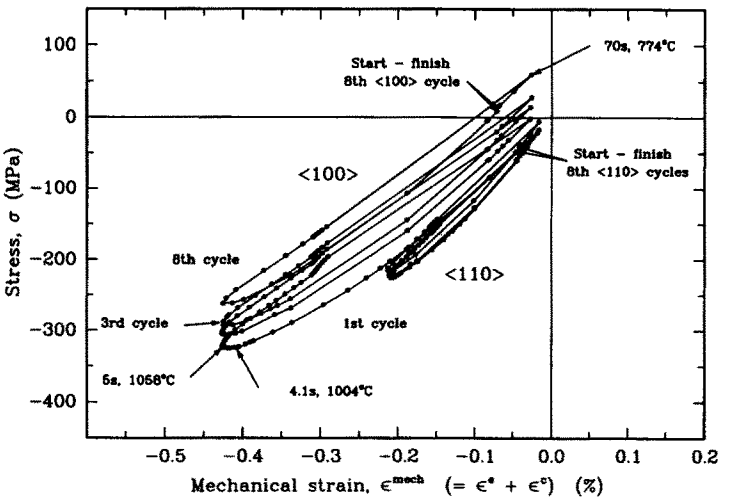

Fig. 11. Anisotropic creep analysis for 6 s heating, 60 s hold with: (a) 15 s cooling; (b) 7 s cooling.

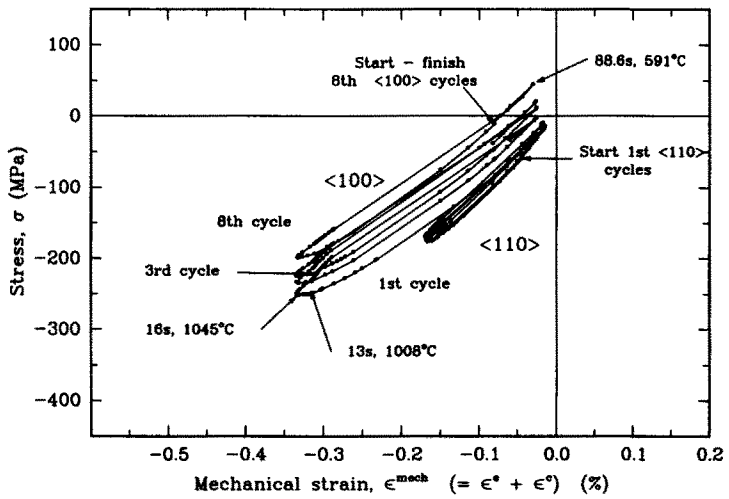

Fig. 12. Anisotropic creep analysis for 20 s heating, 60 s hold and 15 s cooling.

inspired model is proposed. Since the mean mechanical strain remains constant, the decrease in elastic strain is the increase in creep strain. The shifting of the stresses per cycle, $d\sigma/dN$, will then be proportional to the creep strain accumulated during each cycle ε^c, which is in turn proportional to the creep rate divided by the cycling rate, $\dot{\varepsilon}^c/\dot{N}$. In turn, $\dot{\varepsilon}^c$ has an approximate power law dependence on stresses (13)

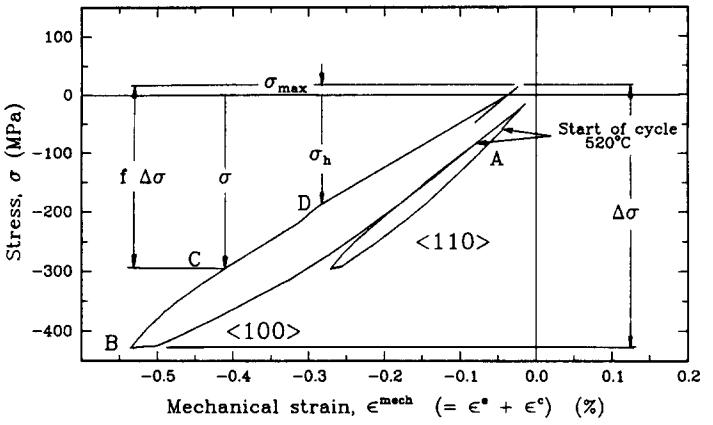

Fig. 13. Parameters used from the first cycle to estimate σ_{max}.

Table 4. Changes in σ_{max} with cycles for ⟨100⟩ (eqn (24))

Heating time (s)	Cooling time (s)	$\sigma_{max}(1)$ (MPa)	$\Delta\sigma$ (MPa)	f	C	m	σ_{max} (MPa) for cycle No. 100	500	6000	Steady state
4.5	15	13.1	441	0.73	0.09	6.8	168	205	245	321
				0.45						201
				1.00						441
6	15	−2	323	0.80	0.08	6.2	134	167	203	258
6	7	49	374	0.83	0.07	6.1	181	215	251	309

$$\frac{d\sigma}{dN} \propto -E\varepsilon^c \propto -\frac{E\dot{\varepsilon}_0}{\dot{N}}\left|\frac{\sigma}{\sigma_0}\right|^m \operatorname{sgn}(\sigma). \tag{22}$$

Consider the stress at that point in the cycle which will have zero stress at steady state (Point C in Fig. 13). Express σ in terms of the changing peak cooling stress σ_{max}, and a fraction f of the total stress range $\Delta\sigma$ (which remains nearly constant during cycling), as shown in Fig. 13

$$\sigma = \sigma_{max} - f\Delta\sigma. \tag{23}$$

Using eqn (23) to integrate expression (22) leads to an expression for σ_{max} in terms of the above variables plus the maximum cooling stress at the end of the first cycle $\sigma_{max}(1)$, and two unknown constants: the creep exponent m, and a constant C, which reduces to the proportion of the creep strain to the elastic strain for the first cycle $[\dot{\varepsilon}^c(1)/\dot{N}]/\varepsilon^e(1)$

$$\sigma_{max}(N) = [\sigma_{max}(1) - f\Delta\sigma(1)][1 + (m-1)C(N-1)]^{-1/(m-1)} + f\Delta\sigma. \tag{24}$$

Equation (24) is based on a stress σ which shifts towards zero as cycles accumulate. At steady state ($\sigma = 0$), compressive creep (before the stress in the cycle reaches zero) generated during the heating and part of the holding period is counteracted by tensile creep (after the stress in the cycle reaches zero, toward the end of the holding period). The point in the cycle which would go to zero stress at steady state would thus be somewhere in between B and D in Fig. 13, since both forward and backward creep would take place within this region.

The parameter f in eqn (24) allows us to estimate the possible values of σ_{max} at steady state. For example, assuming steady state to occur when σ, defined at half-way between the peak compressive stress σ_{min} and the stress at the end of the holding period σ_h (Point C in Fig. 13), reached zero gives the values of f shown in Table 4. With f chosen, and $\sigma_{max}(1)$ and $\Delta\sigma$ known, C and m from eqn (24) can be evaluated from the calculated transients of

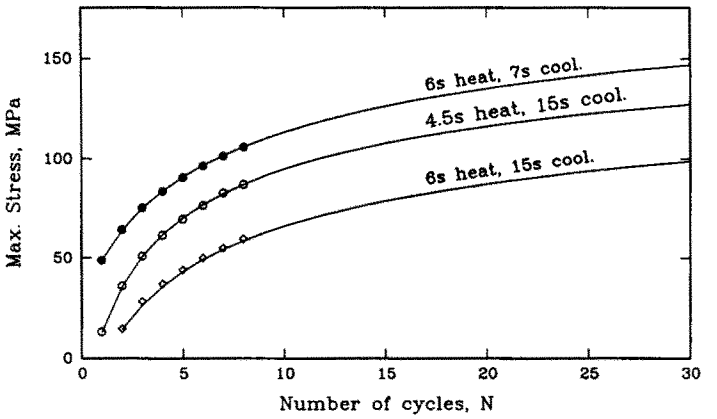

Fig. 14. Changes in the peak stresses encountered during cooling according to eqn (24).

each thermal cycle (Figs 10(c)–12). Figure 14 shows least square curve fittings to eqn (24) for the 4.5 s heating and for the 6 s heating histories with two different cooling rates. Table 4 shows the resulting constants C and m and how σ_{max} increases with cycling from eqn (24). Most of the rise in σ_{max} for the three histories reaches 2/3 of its final value before the first 500 cycles.

Different values of f were chosen to evaluate its effect on σ_{max}. At one extreme, take the point in the cycle at which $\sigma = 0$ at steady state to be the stress at the *end* of the holding period (Point D in Fig. 13). In this case, for the 4.5 s history (Fig. 10(b)), $f = 0.45$. The above procedure then gave a stress at steady state of $\sigma_{max} = 201$ MPa (against 321 MPa for $f = 0.73$ when σ is at half-way from compressive peak to hold). At the other extreme, for σ at the compressive peak, $f = 1$, giving $\sigma_{max} = 441$ MPa.

While the half-way basis for f in Table 4 was somewhat arbitrary, we think that a computer solution for σ_{max} at steady state (if it were feasible) would be lower than that of Table 4 by 10–30%. In any event, it is clear that the tensile stresses appear early in the 6000 cycle life.

(5) The ⟨110⟩ orientation exhibits ratcheting similar to the ⟨100⟩ but less pronounced. It, also, shows no changes in the strain range.

(6) From all the preceding discussion, the thermo-elastic analysis was very good at estimating the strain ranges, but it badly underestimated the σ_{max} obtained from the creep analysis (e.g. −20 MPa vs 245 MPa after 6000 cycles for the 4.5 s heating history at a ⟨100⟩ location).

4.2. *Coating*

The effect of the strain on the coating life is again reflected only in the mechanical part of the total strain, since the thermal strains will not by themselves cause damage. The mechanical strain ranges (as absolute values) for the coating were obtained by adding the thermal expansion mismatch strain range (0.31%), which only depends on α_s, α_c, and the extreme cycle temperature, to those of the substrate

$$\Delta\varepsilon_c^{mech} = \Delta\varepsilon_s^{mech} + (\alpha_c - \alpha_s)\,\Delta T \quad \text{for constant } \alpha, \text{ or} \tag{25}$$
$$= \Delta\varepsilon_s^{mech} + \Delta[\alpha_c(T - T_{ref}) - \alpha_s(T - T_{ref})].$$

For instance, for the most severe cycle with a mechanical strain range for the substrate of $\Delta\varepsilon_{subs}^{mech} = 0.52\%$ (Table 3), the coating range is $\Delta\varepsilon_{coat}^{mech} = 0.83\%$.

The coating crack initiation life is driven not only by the mechanical strain range but also by the stresses. A finite element analysis of the coating was carried out to evaluate these stresses. The accuracy of the finite element analysis was set by a nodal force tolerance for equilibrium of 0.1 N (for a 0.05 mm^2 element section), and by a maximum change in the equivalent tensile plastic strain during an increment of 10^{-5}. The initial residual stress in the coating was tentatively assumed to be zero. (As shown below, initial residual stresses,

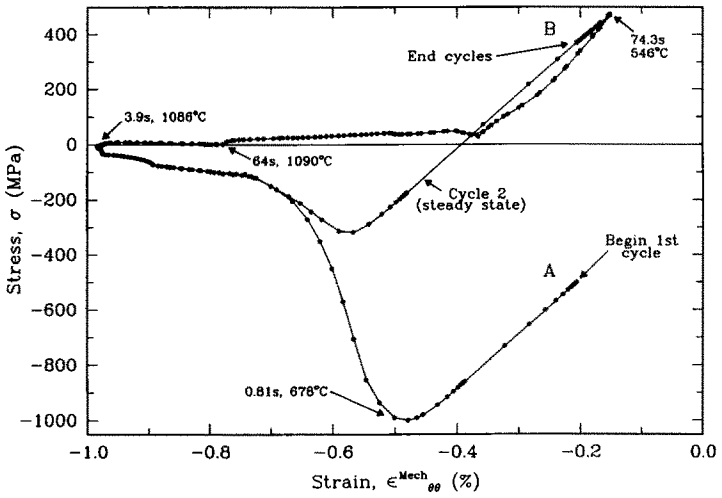

Fig. 15. Hysteresis loop for NiCoCrAlY coating for the 4.5 s heating, 60 s hold, and 15 s cooling cycle. (Imposed displacements from ⟨100⟩ substrate.)

due to the aging treatments and their change due to further relaxation and differential contraction on cooling, would disappear after the first cycle.) An estimate of the shear stresses on the coating/substrate interface due to centrifugal forces in a turbine blade gave only 0.4 MPa, which turns out to be negligible.

With zero initial stress, heating to 520°C gives a compressive stress at the beginning of the first cycle (Point A of Fig. 15). Subsequently, the high creep rates make the stresses relax almost to zero during the first 3 s of the heating period. Steady state is approximately reached in the second cycle (Fig. 15) due to the fact that the forward creep generated when $\sigma < 0$ is offset by backward creep generated mainly during the beginning of cooling. The breaks in the slope during the cycles are due to the discrete creep data input into the finite element model.

The negligible effect of an initial residual stress can now be seen. Any residual stress could not have shifted the stress at the start of the first cycle (520°C) any higher than Point B, because the tensile stress would have exceeded yield. Any initial stress starting the cycle between A and B would converge to steady state even faster than the zero initial stress corresponding to Point A.

The maximum tensile stress in the coating, $\sigma^c_{max} = 460$ MPa (compared to 245 MPa for 6000 cycles for the substrate, Table 4), is reached at 546 C during cooling (Fig. 15). At this stress and temperature, the coating will be on the verge of yielding (Strangman, 1977). This high coating stress will certainly promote substrate as well as coating cracking, since even after a coating crack propagates to the substrate/coating interface, the high coating stresses will still augment the crack tip stress intensity and hence the propagation rate (unless interface spalling were to occur).

The only crack initiation data found in the literature was that of Leverant *et al.* (1976). For comparative purposes, Fig. 16 shows crack initiation in an NiCoCrAlY coating on various superalloy substrates which were tested with a 67 s heating cycle. Based on these data and on our coated CMSX-3 strain ranges, crack initiation for our simulated service should take place almost immediately. Thermal fatigue tests performed in conjunction with our work (Busso, 1987; Busso and McClintock, 1988), show that coating cracks may not occur before 6000 cycles even with strain ranges of up to 0.51% (Fig. 16),† whereas Leverant *et al.* (1976) reported this limit to be around 0.22%.‡ This discrepancy may be associated with the level of the tensile cooling stresses, and also with different shapes of the hysteresis loops, causing different interactions of stress, strain, and temperature. However, since

† Thermal fatigue tests done by Holmes *et al.* (1987) on an aluminide coating revealed that crack-like defects extending into the substrate required a mechanical strain range for the coating greater than 0.59%.

‡ Other data, unpublished, appear to be closer to our results than to Leverant *et al*'s.

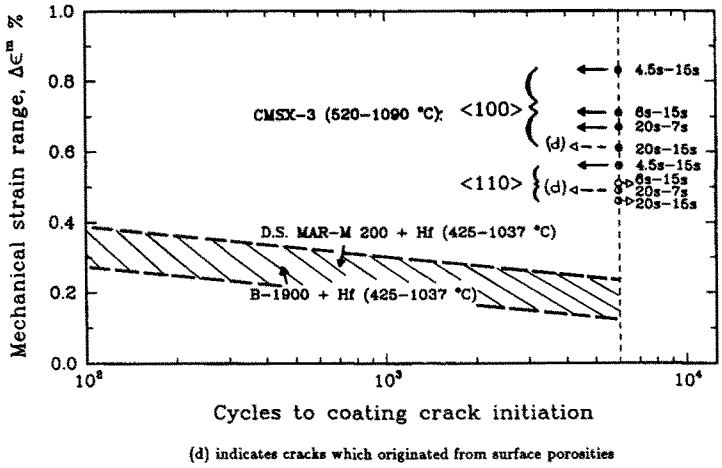

(d) indicates cracks which originated from surface porosities

Fig. 16. Crack initiation in NiCoCrAlY coating on different substrates (Leverant *et al.*, 1976).

Leverant *et al.* (1976) did not report these details, a quantitative comparison cannot be carried out.

To minimize the level of these tensile stresses and strain ranges in the coating, thermal expansion mismatch strains between coating and substrate should be minimized. Beyond that, further crack initiation and crack propagation data for the coating, with realistic stress–strain–temperature histories, are necessary to accurately correlate realistic strain ranges with the development of damage.

5. CONCLUSIONS

(1) The general anisotropic formulation for creep of cubic crystals was obtained in terms of uniaxial ⟨100⟩ and ⟨110⟩ data.

(2) For the substrate, the conventional thermo-elastic analysis is a good predictor of strains and strain ranges, even for cycles with creep. The shape of the hysteresis loops is little affected by creep. Mechanical strain ranges for the ⟨100⟩ substrate orientation vary from 0.52% for the 4.5 s heating cycle to 0.31% for the 20 s heating cycle.

(3) Continued cycling produces ratcheting of the stresses for both crystal orientations but does not affect the strain ranges, which play a role in coating degradation.

(4) Peak tensile stresses generated in the substrate during cooling increase considerably during cycling. This increase was 6–8 times greater for the ⟨100⟩ than for the ⟨110⟩ rim location. A mechanics-inspired model of long time ratcheting revealed that the main effect of different heating rates on cooling peak stresses will be seen before the 500th cycle, when the rise in peak stress reaches 2/3 of its final value for all thermal histories. For the most severe 4.5 s heating time, the peak stress rises from 13 MPa at the first cycle to 245 MPa at the 6000th cycle. These values, compared to the −20 MPa estimated from the conventional thermo-elastic analysis, indicate that the cooling stress levels calculated thermoelastically were highly underestimated, and as a result, their effects in the crack initiation process and subsequent crack propagation rates may be substantial.

A decrease in the cooling times for the 6 s heating cycle from 15 to 7 s (while maintaining the same heating rate) resulted in an increase in the peak cooling stresses from 203 to 251 MPa at the 6000th cycle.

(5) For the coating, to minimize the level of the tensile cooling stresses and strain ranges, thermal expansion mismatch strains between coating and substrate should be minimized. In our case, with α_c typically $1.3\alpha_s$, the most severe imposed substrate strain range (0.53%) induced a 0.83% strain range and 460 MPa tensile cooling stress in the coating. Future work on determining crack initiation and crack propagation data for NiCoCrAlY coatings for the 520–1090°C temperature range is needed to correlate these strain ranges and stresses with the development of damage.

Acknowledgements—Support for this work by the National Science Foundation through grant DMR 84-18718 is gratefully acknowledged. The authors are also very thankful to General Motors–Allison Turbine Division for their support through the donation of the CMSX-3 and the supplying of relevant technical information. All computations were performed on a Data General MV10000 computer donated to MIT by the Data General Corporation. The ABAQUS program was provided under academic license by Hibbitt, Karlsson, and Sorensen Inc., Providence, Rhode Island. The authors are thankful to Prof. David Parks, Allen Lush, and Dr John Holmes for their helpful discussions.

REFERENCES

ABAQUS (1985). A general purpose finite element code with emphasis on non-linear applications, version 4.5. Hibbitt, Karlsson, and Sorensen Inc., Providence, Rhode Island.

Allison, General Motors Turbine Division (1986). Private communication.

Bishop, J. F. and Hill, R. (1951). A theory of the plastic distortion of a polycrystalline aggregate under combined stress. *Phil. Mag.* **42,** 414–427.

Busso, E. P. (1987). Thermal fatigue of an overlay coating for single crystal nickel-base superalloys. M.Sc. thesis, Dept. Mech. Engng, MIT, May.

Busso, E. P. and McClintock, F. A. (1988). Mechanisms of thermal fatigue degradation of an overlay coating. To be submitted to *Mater. Sci. Engng.*

Hebsur, M. G. and Miner, R. V. (1986). High temperature tensile and creep behavior of low pressure plasma-sprayed NiCoCrAlY coating alloy. *Mater. Sci. Engng* **83,** 239–245.

Hill, R. (1950). *The Mathematical Theory of Plasticity*, p. 320. Clarendon Press, Oxford.

Hillery, R. V., Pilsner, B. H., Cook, T. S. and Kim, K. S. (1986). Thermal barrier coating life prediction model. General Electric Co., NASA CR-179504.

Holmes, J. W., McClintock, F. A., O'Hara, K. S. and Conners, M. E. (1987). Thermal fatigue testing of coated monocrystalline superalloys. In *Low-cycle Fatigue* (Edited by H. D. Saloman *et al.*), ASTM STP 942, pp. 672–691.

Howes, M. A. H. (1976). A study of thermal fatigue mechanisms. In *Thermal Fatigue of Materials and Components* (Edited by D. A. Spera and D. F. Mowbray), ASTM STP 612, pp. 86–105.

Kaufman, A. and Halford, G. R. (1984). Engine cyclic durability by analysis and material testing. NASA Technical Memorandum 83577.

Leverant, G. R., Strangman, T. E. and Langer, B. S. (1976). Parameters controlling the thermal fatigue properties of conventionally cast and directionally solidified turbine alloys. In *Superalloys 1976*, pp. 285–295. AIME High Temp. Alloys Committee.

Mackay, R. A., Dreshfield, R. L. and Maier, R. D. (1980). Anisotropy of nickel-base superalloy single crystals. In *Superalloys 1980*, pp. 385–394. AIME High Temp. Alloys Committee.

Nesbitt, J. A., Pilsner, B. H., Carol. L. A. and Heckel, R. W. (1984). Cyclic oxidation behavior of $\beta+\gamma$ overlay coatings on γ and $\gamma+\gamma'$ alloys. In *Superalloys 1984*, pp. 699–710. Met. Soc. AIME.

Rickerby, D. S. and Wood, M. I. (1986). Evaluation of ion plated CoCrAlY and NiCrAlTi coatings for gas turbines. *J. Vac. Sci. Technol.* **A6,** 2557–2570.

Simmons, G. and Wang, H. (1971). *Single Crystal Elastic Constants and Calculated Aggregate Properties.* MIT Press, Cambridge, Massachusetts.

Strangman, T. E. (1977). Fatigue crack initiation and propagation in EB-PVD coatings for gas turbine superalloys. *Thin Solid Films* **45,** 499–506.

Thulin, E. D., Howe, D. C. and Singer, I. D. (1982). Energy efficient engine: high performance turbine detailed design report. NASA Report No. CR-165608, Pratt & Whitney Aircraft Group, East Hartford, Connecticut.